Dynamics of liquid-filled spacecraft

Gerrits, J.; Veldman, A.E.P.

Published in:
Journal of Engineering Mathematics

Publication date:
2003

Journal of Engineering Mathematics **45:** 21–38, 2003.

Dynamics of liquid-filled spacecraft

J. GERRITS* and A.E.P. VELDMAN
Department of Mathematics, University of Groningen, P.O. Box 800, 9700 AV Groningen, The Netherlands (e-mail: veldman@math.rug.nl)

Received 22 May 2002; accepted in revised form 24 September 2002

Abstract. A method is presented for simulating coupled liquid-solid dynamics. An important example of a coupled liquid-solid system is a satellite carrying fuel. The dynamics of the satellite and the onboard fuel influence each other, which may lead to satellite motion that is uncontrollable. For better understanding of the complex dynamics of coupled systems, a numerical model is developed. The model consists of two parts. The first part that solves the liquid motion is only briefly discussed here. The focus in this paper is on the way in which the dynamics of the liquid and the solid body are coupled. For this, the governing equations are presented in which terms appear that represent the force and torque on the solid body due to the sloshing liquid. The governing equations are rewritten such that the discrete approximation of these equations can be integrated in a stable manner for arbitrary liquid/solid mass ratios. Results are presented demonstrating the stability of the present model. A grid-refinement study and a time-step analysis are performed. Finally, the flat-spin motion of a satellite, partially filled with liquid, that flew in 1992 as part of the Wet Satellite Model experiment is studied. Results from the simulation are compared with the actual flight data.

Key words: coupled dynamics, flat spin, liquid sloshing, microgravity

1. Introduction

Usually, in engineering applications, the motion of a container carrying liquid is not prescribed, but follows from an interaction with the liquid motion: the sloshing liquid induces a force and torque on the container, which, as a consequence, starts to accelerate. In return, this container motion influences the liquid motion, and so on. This coupling between the liquid dynamics and the dynamics of the solid body is called dynamical interaction.

Dynamical interaction is often observed when liquid is transported by vehicles. It is well known, for example, that the braking distance of a tank lorry is considerably influenced by the amount of fuel it is carrying [1]. Aboard oil tankers advantage is taken of dynamical interaction: in so-called anti-roll tanks, water sloshes (due to the roll motion of the vessel) such that it stabilises the motion of the tanker [2, 3].

Also in space, aboard satellites carrying fuel, dynamical interaction plays an important role. Regularly, satellites need course corrections to remain in the correct orbit. These are accomplished by firing small thrusters. This, however, will also induce liquid motion and the sloshing liquid may affect the satellite motion, such that the desired course correction may not be accomplished. A recent example of a satellite that got into problems was NASA's NEAR (Near Earth Asteroid Rendezvous) satellite, which in 1998 was on its way to the asteroid 433 Eros [4]. A propellant burn that should have put the spacecraft on track was aborted

*present affiliation: Institute for Marine and Atmospheric Research Utrecht, Utrecht University, P.O. Box 80005, 3508 TA Utrecht, The Netherlands

after sensors detected accelerations that exceeded safety limits programmed into its onboard computer. Further investigation revealed that the spacecraft was tumbling due to sloshing of the onboard liquid. This incident eventually caused a 13 months delay in the mission.

Dynamical interaction in space is a particularly complex problem. Not only because of the complex dynamics of a coupled system, but also because of the poor understanding of liquid behaviour under micro-gravity conditions. However, in order to prevent the future loss of expensive satellites, it is important to improve our knowledge of coupled solid-liquid systems in an extra-terrestrial environment.

In this paper a method is presented for the numerical simulation of coupled solid-liquid dynamics. The method consists of both a model for simulating liquid dynamics in a micro-gravity environment (however, terrestrial liquid dynamics is supported as well) and a model for the solid-body dynamics in which forces and torques due to the sloshing liquid appear. In the latter model the governing equations are written in a suitable reference frame such that the integration is stable for arbitrary solid/liquid mass ratios. The numerical model for the solid-body dynamics is the focus of this paper; the liquid dynamics is discussed only briefly (more details can be found in [5, Chapter 2]). The model has been implemented in a computer program of which results are presented.

2. Liquid dynamics

First the mathematical model for the liquid dynamics is explained. Also, some key aspects of the numerical model are discussed.

2.1. Governing equations

The motion of an incompressible liquid (with density ρ and kinematic viscosity μ) is governed by conservation of mass

$$\nabla \cdot \boldsymbol{u} = 0, \tag{1}$$

and conservation of momentum

$$\frac{\mathrm{D}\boldsymbol{u}}{\mathrm{D}t} = -\frac{1}{\rho}\left(\nabla p - (\nabla \cdot \mu \nabla)\,\boldsymbol{u}\right) + \boldsymbol{F} + \boldsymbol{f}. \tag{2}$$

In these equations p is the pressure, $\boldsymbol{u} = (u, v, w)^T$ is the velocity vector in a moving reference frame (moving with, for example, the satellite) and $\boldsymbol{F}$ is an acceleration due to external forces (gravity in this paper). The vector $\boldsymbol{f}$ is the acceleration due to a virtual body force representing the fact that the equations are written in a moving reference frame. This acceleration can be written as

$$\boldsymbol{f} = -\dot{\boldsymbol{q}} - \dot{\boldsymbol{\omega}} \times \boldsymbol{r} - \boldsymbol{\omega} \times (\boldsymbol{\omega} \times \boldsymbol{r}) - 2\boldsymbol{\omega} \times \boldsymbol{u}, \tag{3}$$

where $\dot{\boldsymbol{q}} = \mathrm{d}\boldsymbol{q}/\mathrm{d}t + \boldsymbol{\omega} \times \boldsymbol{q}$ is the acceleration of the moving origin with respect an inertial reference frame, $\dot{\boldsymbol{\omega}} = \mathrm{d}\boldsymbol{\omega}/\mathrm{d}t + \boldsymbol{\omega} \times \boldsymbol{\omega} = \mathrm{d}\boldsymbol{\omega}/\mathrm{d}t$ is the angular acceleration of the moving reference frame, $\boldsymbol{\omega}$ is the angular velocity of the moving reference frame and $\boldsymbol{r}$ is the position of a liquid particle in the moving reference frame. Note that in the equations above, the vector $\boldsymbol{u}$ is the velocity in the moving reference frame. If the velocity in the inertial reference frame is denoted by $\boldsymbol{v}$, then the following relation holds:

$$\frac{\mathrm{D}\boldsymbol{v}}{\mathrm{D}t} = \dot{\boldsymbol{q}} + \dot{\boldsymbol{\omega}} \times \boldsymbol{r} + \boldsymbol{\omega} \times (\boldsymbol{\omega} \times \boldsymbol{r}) + \frac{\mathrm{D}\boldsymbol{u}}{\mathrm{D}t} + 2\boldsymbol{\omega} \times \boldsymbol{u}. \tag{4}$$

2.2. Features of the numerical model

Since the coupled dynamics is the focus of this paper, the numerical model for the liquid dynamics is discussed very briefly.

2.2.1. *Discretisation*

The continuity equation (1) and Navier-Stokes equations (2) are discretised with a finite-volume method [6] on a staggered, Cartesian grid [7]. Complex geometries are incorporated using the cut-cell technique [8, 9, 10]. The discrete operators for convection and diffusion are constructed such that their symmetry properties correspond to those of the continuous operators, *i.e.*, convection is approximated by a skew-symmetric operator and diffusion is approximated by a symmetric, negative definite operator. Further, the pressure gradient is discretised such that its discrete coefficient matrix is equal to minus the transpose of the discrete divergence operator. With these properties it can be proven that (in the absence of external forces) the discrete kinetic energy cannot grow, which makes the model extremely robust [11].

2.2.2. *Free surface*

The location of the free surface is captured using a Volume-of-Fluid function F^s, which is defined in every computational cell. It denotes whether a cell contains no fluid ($F^s = 0$), is completely filled ($F^s = 1$) or contains part of the free surface ($0 < F^s < 1$). The basic advection algorithm is based on the method of Hirt and Nichols [12]. However, since the original method of Hirt and Nichols creates a lot of 'flotsam' and 'jetsam', the method is adapted with a local height function [13]. In cells that contain part of the free surface (surface cells) a height function is constructed in a block of $3 \times 3 \times 3$ cells. In these surface cells, the free surface is advected by changing the value of the local height function instead of using the method of Hirt and Nichols. By using a local height function most of the 'flotsam' and 'jetsam' is removed. Moreover, this method conserves mass rigorously.

3. Solid-body dynamics

In this section the solid-body dynamics is discussed. First, the governing equations are stated. Hereby, the choice of reference frame is extremely crucial for the stability of the numerical integration as is demonstrated. Thereafter, the solution method is explained.

3.1. Governing equations

The model for the solid-body motion consists of an equation for linear momentum

$$m_s\dot{\boldsymbol{q}} + \dot{\boldsymbol{\omega}} \times m_s\overline{\boldsymbol{r}}_s + \boldsymbol{\omega} \times (\boldsymbol{\omega} \times m_s\overline{\boldsymbol{r}}_s) = \boldsymbol{\mathcal{F}} + m_s\boldsymbol{F}, \tag{5}$$

and an equation for angular momentum

$$m_s\overline{\boldsymbol{r}}_s \times \dot{\boldsymbol{q}} + \boldsymbol{I}_s\dot{\boldsymbol{\omega}} + \boldsymbol{\omega} \times \boldsymbol{I}_s\boldsymbol{\omega} = \boldsymbol{\mathcal{T}} + m_s\overline{\boldsymbol{r}}_s \times \boldsymbol{F}. \tag{6}$$

In these equations $\boldsymbol{q}$ and $\boldsymbol{\omega}$ are the unknown variables, representing the linear and angular velocity of the solid body, respectively. The mass of the solid body is denoted by m_s. Further, $\boldsymbol{I}_s$ is the moment-of-inertia tensor and $\overline{\boldsymbol{r}}_s$ is the centre of mass of the solid body. Note that the latter two quantities are relative to the moving reference frame. These equations can be simplified considerably by setting $\overline{\boldsymbol{r}}_s = 0$. However, the present form is more convenient in the rest of this section where these equations are rewritten in a different coordinate system. The last terms in (5) and (6) represent external forces and torques. Finally, $\boldsymbol{\mathcal{F}}$ and $\boldsymbol{\mathcal{T}}$ are, respectively, the force and torque that the fluid, via pressure (normal stress) and viscous effects (mainly tangential stress), exerts on the boundary of the solid body, *i.e.*,

$$\boldsymbol{\mathcal{F}} = \oint_{\partial V} (p\boldsymbol{E}_3 - \mu\nabla\boldsymbol{u}) \cdot \boldsymbol{n}\,\mathrm{d}S,$$
$$\boldsymbol{\mathcal{T}} = \oint_{\partial V} (\boldsymbol{r} \times (p\boldsymbol{E}_3 - \mu\nabla\boldsymbol{u})) \cdot \boldsymbol{n}\,\mathrm{d}S.$$

Here, $\boldsymbol{E}_3$ is the 3×3 identity matrix and $\boldsymbol{n}$ the outward pointing normal on the boundary ∂V of the total volume V of the solid body. When the divergence theorem is used, these integrals can be written as integrals over the volume V

$$\boldsymbol{\mathcal{F}} = \int_V \nabla p - (\nabla \cdot \mu\nabla)\,\boldsymbol{u}\,\mathrm{d}V = -\int_V \rho\left(\frac{\mathrm{D}\boldsymbol{v}}{\mathrm{D}t} - \boldsymbol{F}\right)\mathrm{d}V,$$
$$\boldsymbol{\mathcal{T}} = \int_V \boldsymbol{r} \times (\nabla p - (\nabla \cdot \mu\nabla)\,\boldsymbol{u})\,\mathrm{d}V = -\int_V \rho\boldsymbol{r} \times \left(\frac{\mathrm{D}\boldsymbol{v}}{\mathrm{D}t} - \boldsymbol{F}\right)\mathrm{d}V.$$

In the last step the Navier-Stokes equations (2) and Equations (3) and (4) were used. Note that this integration in the previous equations is not only over the liquid volume, but also over the void. In the void the density is set to zero, such that the void region does not contribute to the integral.

Direct time integration of the Equations (5) and (6) would result in a method that is not stable for arbitrary liquid/solid mass ratios (this is demonstrated in Section 4). Therefore the system for the solid-body dynamics is rewritten first. Consider $\boldsymbol{\mathcal{F}} = -\int_V \rho\,(\mathrm{D}\boldsymbol{v}/\mathrm{D}t - \boldsymbol{F})\,\mathrm{d}V$ in the right-hand side of Equation (5). Using relation (4) for the liquid velocity $\boldsymbol{v}$ in an inertial reference frame and the liquid velocity $\boldsymbol{u}$ in a moving reference frame, the force $\boldsymbol{\mathcal{F}}$ is rewritten as

$$\boldsymbol{\mathcal{F}} = -\int_V \rho\left(\dot{\boldsymbol{q}} + \dot{\boldsymbol{\omega}} \times \boldsymbol{r} + \boldsymbol{\omega} \times (\boldsymbol{\omega} \times \boldsymbol{r}) + \frac{\mathrm{D}\boldsymbol{u}}{\mathrm{D}t} + 2\boldsymbol{\omega} \times \boldsymbol{u} - \boldsymbol{F}\right)\mathrm{d}V.$$

Since the linear velocity $\boldsymbol{q}$ and the angular velocity $\boldsymbol{\omega}$ of the solid body are constant over the volume V, this is equal to

$$\boldsymbol{\mathcal{F}} = -\dot{\boldsymbol{q}}\int_V \rho\,\mathrm{d}V - \dot{\boldsymbol{\omega}} \times \int_V \rho\boldsymbol{r}\,\mathrm{d}V - \boldsymbol{\omega} \times \left(\boldsymbol{\omega} \times \int_V \rho\boldsymbol{r}\,\mathrm{d}V\right) - \int_V \rho\left(\frac{\mathrm{D}\boldsymbol{u}}{\mathrm{D}t} + 2\boldsymbol{\omega} \times \boldsymbol{u} - \boldsymbol{F}\right)\mathrm{d}V.$$

In short, denoting the liquid mass with m_l and the centre of mass of the liquid with $\overline{\boldsymbol{r}}_l$ (with respect to the moving reference frame), this can be written as

$$\boldsymbol{\mathcal{F}} = -m_l\dot{\boldsymbol{q}} - \dot{\boldsymbol{\omega}} \times m_l\overline{\boldsymbol{r}}_l - \boldsymbol{\omega} \times (\boldsymbol{\omega} \times m_l\overline{\boldsymbol{r}}_l) - \int_V \rho \left(\frac{\mathrm{D}\boldsymbol{u}}{\mathrm{D}t} + 2\boldsymbol{\omega} \times \boldsymbol{u} - \boldsymbol{F} \right) \mathrm{d}V.$$

Similarly, the torque $\boldsymbol{\mathcal{T}}$ on the right-hand side of Equation (6) can be rewritten, which results in

$$\boldsymbol{\mathcal{T}} = -m_l\overline{\boldsymbol{r}}_l \times \dot{\boldsymbol{q}} - \boldsymbol{I}_l\dot{\boldsymbol{\omega}} - \boldsymbol{\omega} \times \boldsymbol{I}_l\boldsymbol{\omega} - \int_V \rho\boldsymbol{r} \times \left(\frac{\mathrm{D}\boldsymbol{u}}{\mathrm{D}t} + 2\boldsymbol{\omega} \times \boldsymbol{u} - \boldsymbol{F} \right) \mathrm{d}V,$$

where $\boldsymbol{I}_l$ is the moment-of-inertia tensor of the liquid (with respect to the moving reference frame). Substituting these expressions for $\boldsymbol{\mathcal{F}}$ and $\boldsymbol{\mathcal{T}}$ in the Equations (5) and (6) and rearranging terms gives an alternative form of the model for the solid-body dynamics, namely

$$m\dot{\boldsymbol{q}} + \dot{\boldsymbol{\omega}} \times m\overline{\boldsymbol{r}} + \boldsymbol{\omega} \times (\boldsymbol{\omega} \times m\overline{\boldsymbol{r}}) = -\int_V \rho \left(\frac{\mathrm{D}\boldsymbol{u}}{\mathrm{D}t} + 2\boldsymbol{\omega} \times \boldsymbol{u} - \boldsymbol{F} \right) \mathrm{d}V + m_s\boldsymbol{F}, \tag{7}$$

$$m\overline{\boldsymbol{r}} \times \dot{\boldsymbol{q}} + \boldsymbol{I}\dot{\boldsymbol{\omega}} + \boldsymbol{\omega} \times \boldsymbol{I}\boldsymbol{\omega} = -\int_V \rho\boldsymbol{r} \times \left(\frac{\mathrm{D}\boldsymbol{u}}{\mathrm{D}t} + 2\boldsymbol{\omega} \times \boldsymbol{u} - \boldsymbol{F} \right) \mathrm{d}V + m_s\overline{\boldsymbol{r}}_s \times \boldsymbol{F}. \tag{8}$$

In these equations $m = m_s + m_l$ is the total mass and $\boldsymbol{I} = \boldsymbol{I}_s + \boldsymbol{I}_l$ the moment-of-inertia tensor of the coupled system. The centre of mass of the coupled system is denoted with $\overline{\boldsymbol{r}} = (m_s\overline{\boldsymbol{r}}_s + m_l\overline{\boldsymbol{r}}_l)/m$. Note that the sloshing liquid makes the latter two quantities time dependent.

An important difference between Equations (5) and (6) on the one side and Equations (7) and (8) on the other is the distribution of the solid-body mass and the liquid mass over the left-hand side and right-hand side of the equations. In the former system (5) and (6) the left-hand side contains the mass of the solid body, while on the right-hand side the mass of the liquid, which is moving in the inertial reference frame, appears. Intuitively, one can see that solving this system iteratively, where the left-hand side and right-hand side are evaluated at the new and old time level, respectively, can become unstable if the liquid mass is too large with respect to the mass of the solid body. In the latter system (7) and (8) the total mass of the coupled system, *i.e.*, the sum of the solid-body mass and the liquid mass, appears on the left-hand side. Now, the right-hand side contains the liquid mass in the moving reference frame. In this case, solving this system iteratively can be done in a stable manner, since the liquid mass is always smaller than the total mass of the coupled system. A more detailed stability analysis is presented in Section 4.1.

3.2. Solution method

The temporal discretisation of the equations for linear momentum (7) and angular momentum (8) is straightforward. Both the linear acceleration $\mathrm{d}\boldsymbol{q}/\mathrm{d}t$ and the angular acceleration $\mathrm{d}\boldsymbol{\omega}/\mathrm{d}t$ are discretised at the new time level (indicated by a superscript $n+1$). The linear and angular velocity are discretised at the old time level (indicated by a superscript n). Since the model for the solid-body dynamics is applied after the model for the liquid dynamics has been completed (in the same time step), all the quantities from the liquid model carry a superscript $n+1$. This results in

$$m\frac{\mathrm{d}\boldsymbol{q}}{\mathrm{d}t}^{n+1} + \frac{\mathrm{d}\boldsymbol{\omega}}{\mathrm{d}t}^{n+1} \times m\overline{\boldsymbol{r}}^{n+1} = \boldsymbol{\mathcal{L}}^n, \tag{9}$$

$$m\overline{\boldsymbol{r}}^{n+1} \times \frac{\mathrm{d}\boldsymbol{q}}{\mathrm{d}t}^{n+1} + \boldsymbol{I}^{n+1}\frac{\mathrm{d}\boldsymbol{\omega}}{\mathrm{d}t}^{n+1} = \boldsymbol{\mathcal{A}}^n, \tag{10}$$

where

$$\boldsymbol{\mathcal{L}}^n = -m\boldsymbol{\omega}^n \times \boldsymbol{q}^n - \boldsymbol{\omega}^n \times \left(\boldsymbol{\omega}^n \times m\overline{\boldsymbol{r}}^{n+1}\right) - \int_V \rho \boldsymbol{a}^{n+1}\,\mathrm{d}V + m_s \boldsymbol{F}^{n+1}, \tag{11}$$

$$\boldsymbol{\mathcal{A}}^n = -m\overline{\boldsymbol{r}}^{n+1} \times \left(\boldsymbol{\omega}^n \times \boldsymbol{q}^n\right) - \boldsymbol{\omega}^n \times \boldsymbol{I}^{n+1}\boldsymbol{\omega}^n - \int_V \rho \boldsymbol{r}^{n+1} \times \boldsymbol{a}^{n+1}\,\mathrm{d}V + m_s \overline{\boldsymbol{r}}_s \times \boldsymbol{F}^{n+1}. \tag{12}$$

In these equations $\boldsymbol{a}^{n+1} = \mathrm{D}\boldsymbol{u}^{n+1}/\mathrm{D}t + 2\boldsymbol{\omega}^n \times \boldsymbol{u}^{n+1} - \boldsymbol{F}^{n+1}$. Note that the volume V is the volume of the solid body (recall that the volume integral was deduced, via the divergence theorem, from a boundary integral over the boundary of the solid body); hence this volume V does not carry a superscript, since it does not depend on time. However, in that part of the solid body where liquid is absent, the integrand vanishes, because the density is taken to be zero in the void region.

The implementation of the non-integral terms in Equations (9)–(12) is trivial. The implementation of the remaining terms, although being far from difficult, requires some attention. All these terms are of the form $\int_V \rho\varphi^n\,\mathrm{d}V$ and are discretised as

$$\int_V \rho\varphi^n\,\mathrm{d}V \doteq \sum_{i,j,k} \rho\varphi^n_{i,j,k} F^s_{i,j,k} \delta x_i \delta y_j \delta z_k, \tag{13}$$

where the summation is over all the computational cells, φ is some scalar variable (*e.g.*, $\mathrm{D}u/\mathrm{D}t$), $F^s_{i,j,k}$ is the volume-of-fluid function in cell (i, j, k) and $\delta x_i \delta y_j \delta z_k$ is the volume of this cell. The variable φ is evaluated in cell centres. This means that, sometimes, staggered velocities have to be averaged before they can be evaluated. Note that also the centre of mass $\overline{\boldsymbol{r}}_l$ and the moment-of-inertia tensor $\boldsymbol{I}_l$ of the liquid are integral terms, since

$$m_l\overline{\boldsymbol{r}}_l = \int_V \rho\boldsymbol{r}\,\mathrm{d}V \quad \text{and} \quad \boldsymbol{I}_l\boldsymbol{\psi} = \int_V \rho\boldsymbol{r} \times (\boldsymbol{\psi} \times \boldsymbol{r})\,\mathrm{d}V,$$

where $\boldsymbol{\psi}$ is some vector (*e.g.*, $\mathrm{d}\boldsymbol{\omega}/\mathrm{d}t$) the moment-of-inertia tensor operates on. Therefore, these quantities are computed using (13) as well.

In matrix form, the 6×6 linear system consisting of Equations (9) and (10) reads

$$\begin{pmatrix} m & 0 & 0 & 0 & m\overline{r}_z & -m\overline{r}_y \\ 0 & m & 0 & -m\overline{r}_z & 0 & m\overline{r}_x \\ 0 & 0 & m & m\overline{r}_y & -m\overline{r}_x & 0 \\ 0 & -m\overline{r}_z & m\overline{r}_y & I_{xx} & -I_{xy} & -I_{xz} \\ m\overline{r}_z & 0 & -m\overline{r}_x & -I_{xy} & I_{yy} & -I_{yz} \\ -m\overline{r}_y & m\overline{r}_x & 0 & -I_{xz} & -I_{yz} & I_{zz} \end{pmatrix} \boldsymbol{\xi} = \begin{pmatrix} \mathcal{L}_x \\ \mathcal{L}_y \\ \mathcal{L}_z \\ \mathcal{A}_x \\ \mathcal{A}_y \\ \mathcal{A}_z \end{pmatrix}, \tag{14}$$

where $\boldsymbol{\xi} = \left(\mathrm{d}q_x/\mathrm{d}t, \mathrm{d}q_y/\mathrm{d}t, \mathrm{d}q_z/\mathrm{d}t, \mathrm{d}\omega_x/\mathrm{d}t, \mathrm{d}\omega_y/\mathrm{d}t, \mathrm{d}\omega_z/\mathrm{d}t\right)^T$. For presentational reasons the superscripts have been dropped (it will be clear that the matrix and right-hand side are evaluated at time level n, while the unknown vector contains quantities at time level $n + 1$). Further the components of a vector $\boldsymbol{\psi}$ are denoted with subscripts x, y and z, *i.e.*, $\boldsymbol{\psi} = \left(\psi_x, \psi_y, \psi_z\right)^T$, and the moment-of-inertia tensor has components

$$\boldsymbol{I} = \begin{pmatrix} I_{xx} & -I_{xy} & -I_{xz} \\ -I_{xy} & I_{yy} & -I_{yz} \\ -I_{xz} & -I_{yz} & I_{zz} \end{pmatrix}.$$

By Gaussian elimination, the lower-left 3×3 block of the matrix in (14) is eliminated, whence a decoupled system for $\mathrm{d}\boldsymbol{\omega}/\mathrm{d}t$ arises, namely

$$\left(\boldsymbol{I} - m \begin{pmatrix} \overline{r}_y^2 + \overline{r}_z^2 & -\overline{r}_x\overline{r}_y & -\overline{r}_x\overline{r}_z \\ -\overline{r}_x\overline{r}_y & \overline{r}_x^2 + \overline{r}_z^2 & -\overline{r}_y\overline{r}_z \\ -\overline{r}_x\overline{r}_z & -\overline{r}_y\overline{r}_z & \overline{r}_x^2 + \overline{r}_y^2 \end{pmatrix} \right) \begin{pmatrix} \mathrm{d}\omega_x/\mathrm{d}t \\ \mathrm{d}\omega_y/\mathrm{d}t \\ \mathrm{d}\omega_z/\mathrm{d}t \end{pmatrix} = \begin{pmatrix} \mathcal{R}_x \\ \mathcal{R}_y \\ \mathcal{R}_z \end{pmatrix}, \tag{15}$$

where $\mathcal{R}_x = \mathcal{A}_x + \overline{r}_z\mathcal{L}_y - \overline{r}_y\mathcal{L}_z$, $\mathcal{R}_y = \mathcal{A}_y - \overline{r}_z\mathcal{L}_x + \overline{r}_x\mathcal{L}_z$ and $\mathcal{R}_z = \mathcal{A}_z + \overline{r}_y\mathcal{L}_x - \overline{r}_x\mathcal{L}_y$. Note that during this process no divisions (in particular through zero) take place. Using Steiner's theorem, it follows that the 3×3 matrix in (15) is the moment-of-inertia tensor relative to the center of mass of the coupled system. The 3×3 linear system for $\mathrm{d}\boldsymbol{\omega}/\mathrm{d}t$ is solved with Gaussian elimination followed by backward substitution. Once the solution for $\mathrm{d}\boldsymbol{\omega}/\mathrm{d}t$ is known, the solution for $\mathrm{d}\boldsymbol{q}/\mathrm{d}t$ can be found using backward substitution in (14).

In the model for the solid-body dynamics and also in the Navier-Stokes equations the linear and angular velocity of the solid body appears. This means that $\mathrm{d}\boldsymbol{q}^{n+1}/\mathrm{d}t$ and $\mathrm{d}\boldsymbol{\omega}^{n+1}/\mathrm{d}t$ have to be integrated in time, which is done using a fourth-order Runge-Kutta method. To this end, system (14) is rewritten in the form

$$\frac{\mathrm{d}\boldsymbol{y}}{\mathrm{d}t} = \boldsymbol{g}\,(t, \boldsymbol{y})\,, \tag{16}$$

where $\boldsymbol{y} = (\boldsymbol{q}, \boldsymbol{\omega})^T$ and $\boldsymbol{g} = \boldsymbol{M}^{-1}\,(\boldsymbol{\mathcal{L}}, \boldsymbol{\mathcal{A}})^T$. The matrix $\boldsymbol{M}$ is an abbreviation for the matrix that appears in (14). Equation (16) is integrated in time from level n to level $n+1$ by

$$\boldsymbol{y}^{n+1} = \boldsymbol{y}^n + \frac{1}{6}\delta t\,(\boldsymbol{S}_1 + 2\boldsymbol{S}_2 + 2\boldsymbol{S}_3 + \boldsymbol{S}_4)\,,$$

where the four stages $\boldsymbol{S}_1, \ldots, \boldsymbol{S}_4$ are defined as

$$\boldsymbol{S}_1 = \boldsymbol{g}\,(t^n, \boldsymbol{y}^n)\,, \qquad \boldsymbol{S}_2 = \boldsymbol{g}\left(t^n + \frac{1}{2}\delta t, \boldsymbol{y}^n + \frac{1}{2}\delta t\boldsymbol{S}_1\right),$$

$$\boldsymbol{S}_3 = \boldsymbol{g}\left(t^n + \frac{1}{2}\delta t, \boldsymbol{y}^n + \frac{1}{2}\delta t\boldsymbol{S}_2\right), \qquad \boldsymbol{S}_4 = \boldsymbol{g}\left(t^n + \delta t, \boldsymbol{y}^n + \delta t\boldsymbol{S}_3\right).$$

Note that the explicit time dependence in the right-hand side of (16) (*i.e.*, the first argument of the function $\boldsymbol{g}$) is entirely due to the liquid model. Since the models for the liquid dynamics and the solid-body dynamics are treated separately, it is most unconvenient to evaluate the position and velocity of the liquid at the intermediate time level $n+\frac{1}{2}$. Moreover, the quantities of the liquid model are already known at time level $n+1$. Hence, in the Runge-Kutta stages $\boldsymbol{S}_1, \ldots, \boldsymbol{S}_4$, the first argument of $\boldsymbol{g}$ is frozen at time level $n+1$.

In the simulations that have been performed with the method presented in this paper, the solid-body dynamics turns out to be more sensitive to small disturbances than the model for the liquid dynamics, hence requiring either a smaller time step or a more accurate time-integration method. Since the latter option has been implemented, in practice, it is possible to set the time step for the solid-body model equal to the one used in the liquid model. Should this not be

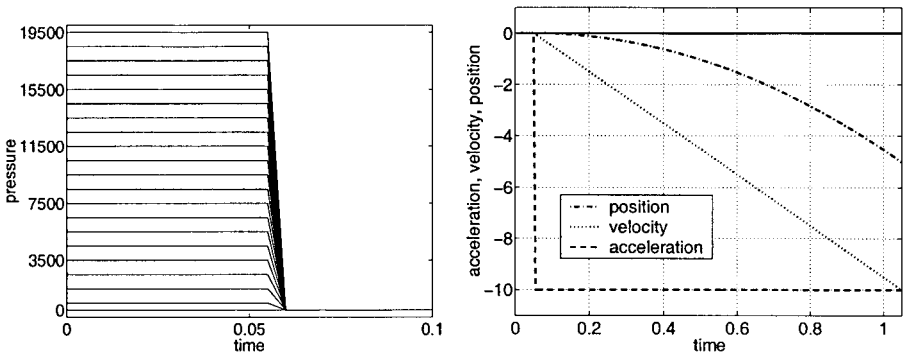

Figure 1. Left: pressure [N/m^2] at equidistant locations along the z-centerline of the tank as a function of time [s]. Right: acceleration [m/s^2] (dashed), velocity [m/s] (dotted) and position [m] (dash-dotted) in z-direction of the coupled system as a function of time [s]. The solid line represents the same quantities in x- and y-directions.

sufficient, then it is possible to take multiple Runge-Kutta time steps during one single time step in the liquid model.

4. Results

The method presented in this paper has been implemented in a computer program. Some results of the present method are discussed in this section. First, the free fall of a container partially filled with fluid is considered for studying the stability of the method. Then, a grid-refinement study and a time-step analysis is performed and the effect of the liquid/solid mass ratio is studied, followed by the simulation of a flat-spin motion of a rectangular container partially filled with liquid. Finally, the Wet Satellite Model experiment is introduced and simulated.

4.1. Free fall

As a first example, the free fall of a rectangular tank partially filled with liquid is simulated using the model (7) and (8), with which no stability problems are expected. Consider a hollow, rectangular tank of dimensions $1 \times 2 \times 4$ m^3 with mass $m_s = 2000$ kg. The lower half (in z-direction) of the tank (*i.e.*, with height $h = 2$ m) is filled with liquid having a mass $m_l = 4000$ kg (which corresponds to a density $\rho = 1000$ kg/m^3). The acceleration $\boldsymbol{F}$ due to gravity is set to $(0, 0, -g)^T$ with $g = 10$ m/s^2.

During the first 0·05 seconds of the simulation (on a computational grid of $10 \times 20 \times 40$ cells) the tank is kept at its initial position, whence the pressure settles itself at hydrostatic values, which serves as a simple test for the liquid model. After 0·05 seconds the tank, together with the liquid, is released. This, of course, causes the coupled system to fall in the negative z-direction with an acceleration equal to gravitational acceleration. Also, the pressure becomes equal to the ambient pressure $p_0 = 0$ N/m^2 everywhere in the fluid, since the coupled system is in a free fall. These results are confirmed in Figure 1. On the left in this figure, the pressure, at equidistant locations along the centreline in z-direction, is plotted. At the bottom of the tank, the pressure is equal to $p = \rho g h = 1000 \times 10 \times 2 = 20000$ N/m^2. Taking into account that the centre of the first computational cell lies half a mesh size (which is $\delta z/2 = 0{\cdot}05$ m) above the bottom of the tank, the maximum value of $p = 19500$ N/m^2 in Figure 1 can be

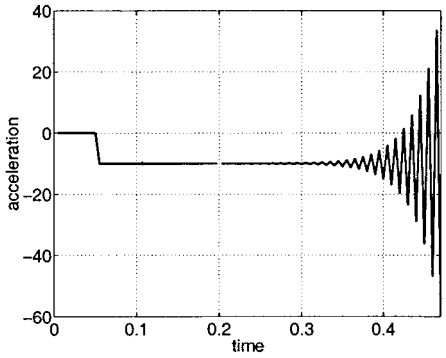

Figure 2. Acceleration [m/s^2] in z-direction of the coupled system as a function of time [s] as predicted by the unstable method.

explained. The same reasoning applies to the centre of the last cell below the free surface, where the pressure is equal to $p = 500$ N/m^2 (at the free surface the pressure has a value of $p = p_0 = 0$ N/m^2). Since the tank is kept at its initial position until $t = 0{\cdot}05$ s the pressure in the tank does not change in this interval. Also, one time step after $t = 0{\cdot}05$ s (the time step is set to $\delta t = 0{\cdot}005$ s) the pressure has not changed, since, in the liquid model, the virtual body force (3) is discretised at the old time level, at which time the tank was not moving. In the next time step, at $t = 0{\cdot}06$ s, the fluid 'feels' that the tank is falling with an acceleration of $\mathrm{d}\boldsymbol{q}/\mathrm{d}t = (0, 0, -10)^T$ m/s^2, whence the pressure in the fluid becomes zero everywhere. On the right in Figure 1 the motion of the tank is plotted. Most of the quantities, namely the angular acceleration, velocity and position in all three spatial directions, are equal to zero during the entire simulation. The linear acceleration (in z-direction) changes from 0 m/s^2 to -10 m/s^2 at $t = 0{\cdot}05$ s as expected. Also the linear velocity and position, showing linear and quadratic behaviour, are plotted. Note that, for presentational reasons, the initial position of the tank is set to zero in this figure.

The previous simulation has been performed with the possibly unstable method (5) and (6) as well. For this method the acceleration of the coupled system with a liquid/solid mass ratio of 1·2 is shown in Figure 2. If the liquid/solid mass ratio is further decreased to lower than one, then the unstable method gives the same results as the stable method. This can be explained by analysing Equations (5) and (7). In the absence of angular motion these equations reduce to

$$m_s \frac{\mathrm{d}\boldsymbol{q}}{\mathrm{d}t} = -\int_V \rho \left(\frac{\mathrm{D}\boldsymbol{v}}{\mathrm{D}t} - \boldsymbol{F} \right) \mathrm{d}V + m_s \boldsymbol{F},$$

and

$$m \frac{\mathrm{d}\boldsymbol{q}}{\mathrm{d}t} = -\int_V \rho \left(\frac{\mathrm{D}\boldsymbol{u}}{\mathrm{D}t} - \boldsymbol{F} \right) \mathrm{d}V + m_s \boldsymbol{F},$$

respectively, (in this case Equation (4) simplifies to $\mathrm{D}\boldsymbol{v}/\mathrm{D}t = \mathrm{d}\boldsymbol{q}/\mathrm{d}t + \mathrm{D}\boldsymbol{u}/\mathrm{D}t$). These equations are discretised by evaluating the left-hand side at the new time level $n + 1$ and the right-hand side at the old time level n, *i.e.*,

$$m_s \frac{\mathrm{d}\boldsymbol{q}}{\mathrm{d}t}^{n+1} = -\int_V \rho \left(\frac{\mathrm{D}\boldsymbol{v}^n}{\mathrm{D}t} - \boldsymbol{F} \right) \mathrm{d}V + m_s \boldsymbol{F},$$

and

$$m\frac{\mathrm{d}\boldsymbol{q}}{\mathrm{d}t}^{n+1} = -\int_V \rho\left(\frac{\mathrm{D}\boldsymbol{u}^n}{\mathrm{D}t} - \boldsymbol{F}\right)\mathrm{d}V + m_s\boldsymbol{F}.$$

If both the liquid velocity $\boldsymbol{u}$ in the moving reference frame and the pressure p vanish throughout the liquid (as is the case in this section), then these equations simplify to

$$m_s\frac{\mathrm{d}\boldsymbol{q}}{\mathrm{d}t}^{n+1} = -m_l\frac{\mathrm{d}\boldsymbol{q}}{\mathrm{d}t}^{n} + m_l\boldsymbol{F} + m_s\boldsymbol{F} \quad \text{and} \quad m\frac{\mathrm{d}\boldsymbol{q}}{\mathrm{d}t}^{n+1} = m_l\boldsymbol{F} + m_s\boldsymbol{F},$$

or

$$\frac{\mathrm{d}\boldsymbol{q}}{\mathrm{d}t}^{n+1} = -\frac{m_l}{m_s}\left(\frac{\mathrm{d}\boldsymbol{q}}{\mathrm{d}t}^{n} - \boldsymbol{F}\right) + \boldsymbol{F} \quad \text{and} \quad \frac{\mathrm{d}\boldsymbol{q}}{\mathrm{d}t}^{n+1} = \boldsymbol{F}.$$

Clearly, the solution for both formulations is $\mathrm{d}\boldsymbol{q}/\mathrm{d}t \equiv \boldsymbol{F}$. However, small disturbances in the solution for $\mathrm{d}\boldsymbol{q}/\mathrm{d}t$ at time level n are in the first formulation amplified with a factor m_l/m_s (this factor is visible in Figure 2, where $m_l/m_s = 1{\cdot}2$), which becomes unstable if the liquid/solid mass ratio exceeds unity in correspondence with the numerical results. Note that this instability can not be solved by decreasing the time step in the Runge-Kutta method for solving system (16). Indeed, the first method is unstable for every time step if $m_l/m_s > 1$.

4.2. Full tank

In this section the angular motion of a container with mass $m_s = 12$ kg and moment-of-inertia tensor $\boldsymbol{I}_s = \mathrm{diag}\,(1, 2, 4)$ kg m^2 is studied. The container is completely filled with liquid. A simple calculation shows that the moment-of-inertia tensor of the liquid in this case is equal to $\boldsymbol{I}_l = \frac{1}{12}m_l\mathrm{diag}\left(\frac{7}{2} - 2\sqrt{2}, \frac{3}{2}, \frac{7}{2} - \sqrt{2}\right)$ kg m^2. The liquid mass is chosen as $m_l = 120$ kg (*i.e.*, a liquid/solid mass ratio of 10) and the initial angular velocity of the system is set to $\boldsymbol{\omega}(0) = (3, 2, 1)^T$ s^{-1}. The coupled system settles itself in a state of minimum kinetic energy, which corresponds to rotation around the axis with maximum moment of inertia (the fluid is responsible for damping the rotation around the x- and y-axes). Thus, in the steady-state solution, the system rotates around the z-axis only. The results for this particular simulation are shown in Figure 3. On the left, the angular velocities around the x-, y- and z-axis are plotted versus time as well as the theoretically predicted final angular velocity around the z-axis. On the right, the projection of the angular velocity on the unit sphere is plotted. From these figures the transition to rotation around a single axis becomes very clear. The numerical simulation predicts a final angular velocity around the stable moment-of-inertia axis in close correspondence with the theoretical value (which follows from conservation of angular momentum); the difference is less than half a percent.

4.2.1. *Grid-refinement and time-step analysis*

The above simulation is repeated on grids consisting of $20\times20\times20$, $40\times40\times40$, $60\times60\times60$ and $80 \times 80 \times 80$ computational cells. The results are shown in Figure 4 (for presentational reasons only the angular velocity around the x-axis on the four different grids is considered). On the right in this figure the solutions on subsequent grids are subtracted from each other, giving an indication of the error in the numerical solution. Clearly, the error decreases when the grid is refined. Note that the large size of the error can be explained by the phase difference between the solutions on the various grids.

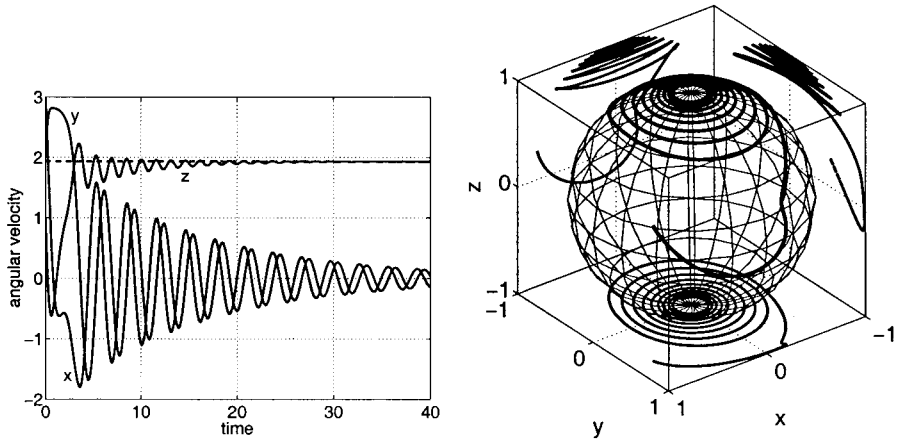

Figure 3. Left: evolution of the angular velocity [s^{-1}] (solid lines) around the three Cartesian axes for a completely filled tank. The dashed line represents the theoretically predicted final angular velocity around the z-axis. Right: projection of the angular velocity on the unit sphere.

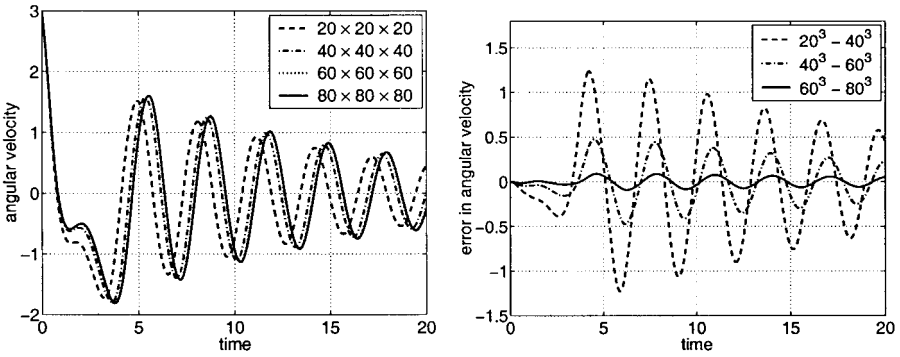

Figure 4. Left: angular velocity [s^{-1}] around x-axis of a full tank for different grids. Right: indication of the error in the angular velocity given by the difference in the solutions on subsequent grids.

All the simulations in this section have been performed with a time step of $\delta t = 10^{-3}$ s. In Figure 5, the previous simulation is repeated on a grid of $40 \times 40 \times 40$ cells but with different time steps, namely $\delta t = 5 \times 10^{-3}$ s, $\delta t = 1 \times 10^{-3}$ s and $\delta t = 2 \times 10^{-4}$ s. The right-hand figure shows that the error in the angular velocity decreases when the time step is reduced.

4.2.2. *Liquid/solid mass ratio*

Since the grid-refinement study and the time-step analysis revealed that the method is consistent, it is possible to examine how the coupled system that has been examined in this section reacts to a change in physical parameters, such as the liquid/solid mass ratio. In the previous simulations the liquid/solid mass ratio was equal to 10; the liquid mass and the solid-body mass were set to $m_l = 120$ kg and $m_s = 12$ kg, respectively. If the liquid/solid mass ratio is increased (by increasing the density of the fluid) the fluid has more influence on the motion of the coupled system, whence the system settles itself faster into a steady state. This phenomenon is illustrated on the left in Figure 6, where the angular velocity of the coupled system is shown for liquid/solid mass ratios of 0·1, 1, 10 and 100. Note that the angular velocity converges to different values for different mass ratios, which is caused by a change in the liquid mass and thus the moment-of-inertia tensor. For presentational reasons only a detail of the time history

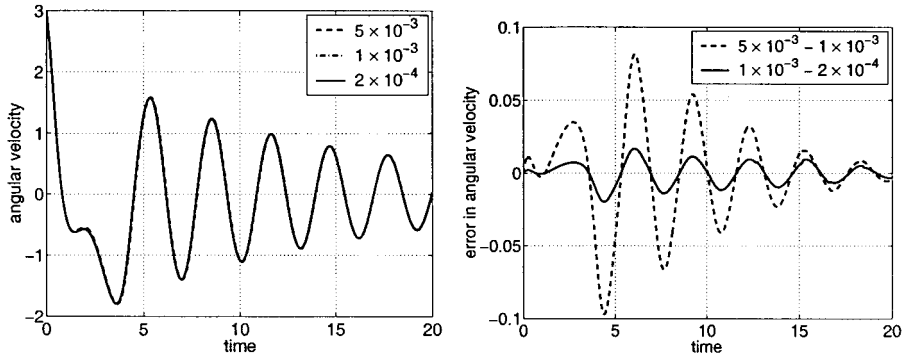

Figure 5. Same as Figure 4 but now for different time steps.

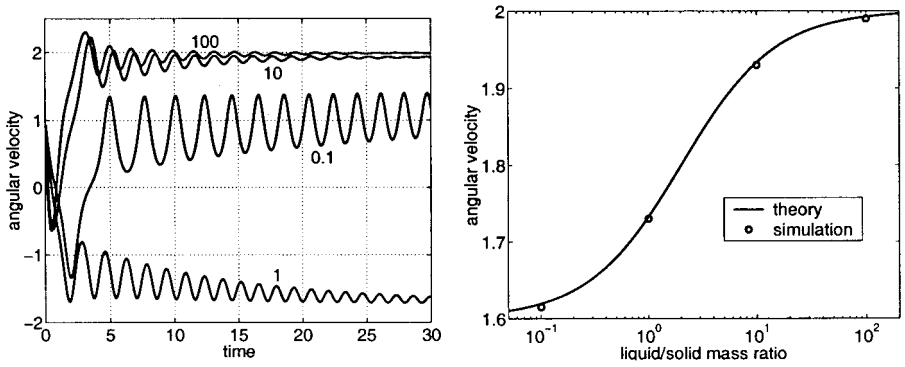

Figure 6. Left: evolution of the angular velocity [s^{-1}] around z-axis of a full tank for different liquid/solid mass ratios. Right: comparison of the theoretical and numerical final angular velocity [s^{-1}] around z-axis.

of the angular velocity is shown in this figure. In the actual simulation the computation was continued until the amplitude of the oscillations in the angular velocity around the z-axis was less than 10^{-2} s (for the simulation with a mass ratio of 0·1 this happened after approximately 400 seconds simulation time). On the right in Figure 6 the computed angular velocity in the steady-state solution is compared to theory. Only the absolute value of the angular velocity is considered, since the coupled system may be rotating in either positive or negative direction in the body-fixed coordinate system. The difference between simulation and theory is less than half a percent for all four mass ratios.

4.3. Partially filled tank

After having studied a completely filled tank, a partially filled tank is discussed in this section. As an example a flat-spin motion is simulated. The same rectangular container that has been studied before is rotating around the x-axis with angular velocity $\omega_x = 5$ s^{-1} (initially, both ω_y and ω_z are equal to zero). The container is filled with fluid for $|y| \geq c$, where c [m] determines the filling ratio. Since $I_{xx} < I_{yy} < I_{zz}$, rotation around the x-axis and z-axis is stable. However, because of the viscous liquid, kinetic energy is dissipated. Hence, in the steady state, the system will be rotating around the z-axis only, which corresponds to a state of minimum kinetic energy. This phenomenon – transition from rotation around the axis with minimum moment of inertia to rotation around the axis with maximum moment of inertia – is known as a flat spin. In the computation the filling ratio was set to 65% and the

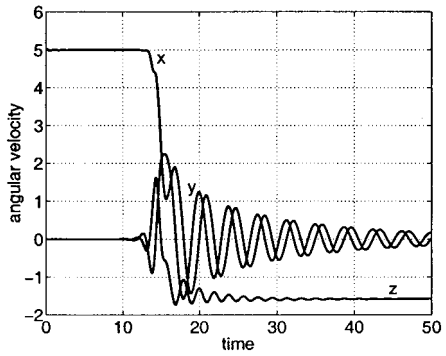

Figure 7. Evolution of the angular velocity [s^{-1}] around the three Cartesian axes for a partially filled tank.

density of the fluid was chosen such that the liquid/solid mass ratio equals $m_l/m_s = 10$. In Figure 7 the angular velocities around the Cartesian axes are shown as a function of time. This figure clearly shows that some time (more than ten seconds) is needed before the transition is triggered. Once rotation around the y- and z-axes is excited, the change of rotation axis takes place in about ten seconds, although quite some time passes before the angular velocities around the x- and y-axes decrease to zero.

In Figure 8 a more detailed study of the steady rotation around the x-axis at the beginning and around the z-axis at the end of the simulation is shown. In this figure snapshots of the free surface (solid lines) are drawn; on the left the results from the simulation and on the right the corresponding plots based on theory are shown. The results in two different cross sections, namely in the xy- and the yz-plane, and at two different time levels, namely at the beginning and at the end of the simulation, are presented. This figure clearly shows that initially the system is rotating around the x-axis and finally around the z-axis. Indeed, in the xy-plane the shape of the free surface changes from a straight line into a circle, while in the yz-plane the opposite behaviour takes place.

When the system is rotating around one axis only, *i.e.*, at the beginning and at the end of the simulation, it is easy to compare the pressure contours to theory, since in this case the pressure contours are concentric circles around the centre of rotation. If the pressure at the free surface is equal to zero, then the pressure p at a distance R from the centre of rotation is equal to

$$p = \frac{1}{2}\rho\,\omega^2\left(R^2 - r^2\right),$$

where ρ is the density of the fluid, ω is the angular velocity and r is the distance between the free surface and the centre of rotation. This theory is compared to the results from the numerical simulation in Figure 8 as well, where the pressure contours are plotted as dashed lines. The correspondence between simulation and theory is very good.

In Figure 9 three-dimensional snapshots of a flat-spin simulation are shown for which the filling ratio was decreased to 40%. In the upper-left snapshot the container is rotating steadily around the axis of minimum moment of inertia. In the second snapshot the beginning of the flat spin can be seen; liquid starts to flow due to rotation around the y- and z-axes. Some intermediate snapshots show the violent behaviour of the transition. Finally, in the bottom-right snapshot, the angular velocities around the x- and y-axes have vanished and the container is rotating steadily around the axis of maximum moment of inertia.

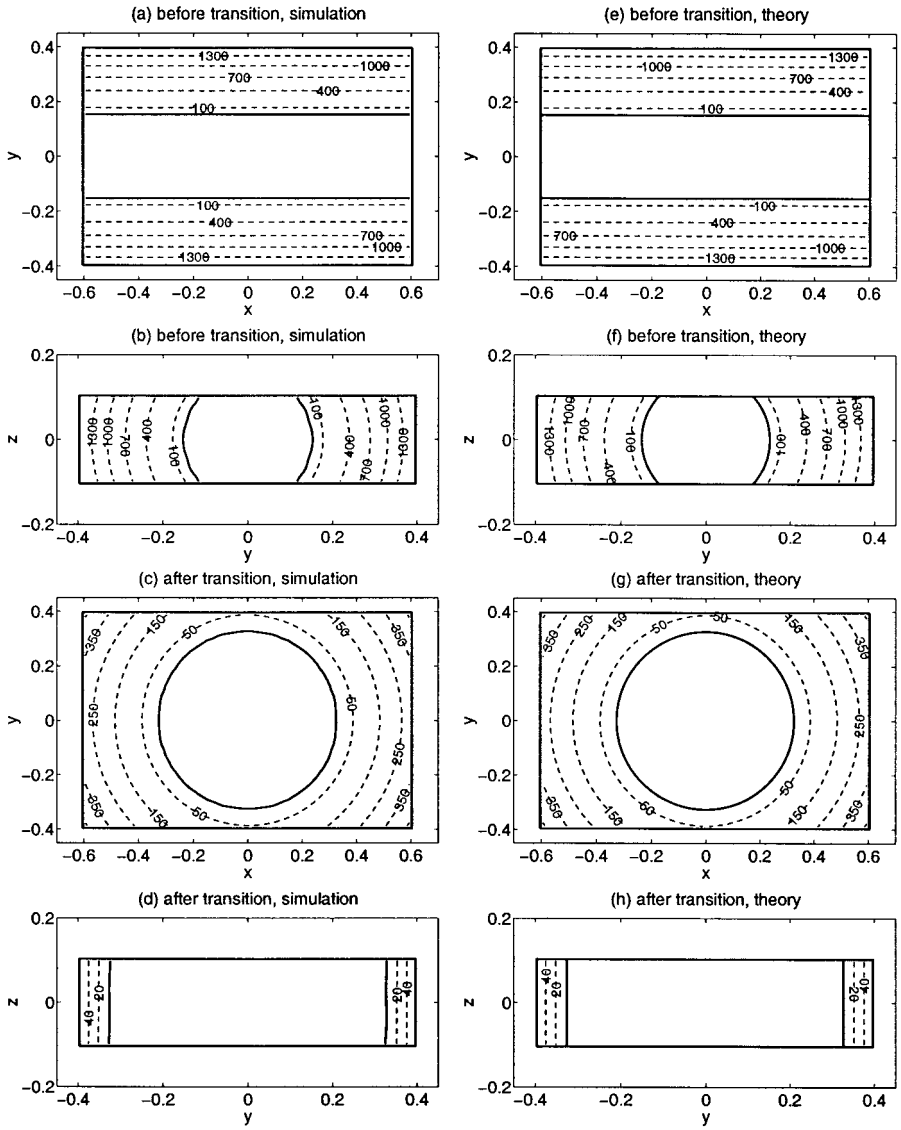

Figure 8. Snapshots of the free surface (solid lines) and pressure contours [N/m^2] (dashed lines) for the flat-spin motion in the xy- and yz-planes at two different time levels, namely at the beginning (top four) and at the end (bottom four) of the flat spin. On the left, results from the simulation; on the right, results based on theory.

4.4. The Wet Satellite Model experiment

For studying the dynamics of a liquid-filled spacecraft, the Wet Satellite Model (WSM) experiment was performed in 1992 [14]. Following the launch of the MASER 5 rocket on April 9, 1992, a small spacecraft, the Ejectable Ballistometer (EB), was separated from the MASER payload. After separation the EB continued on its own trajectory until impact with earth after 370 seconds. Two photographs of the launch of the EB are shown in Figure 10. During its lifetime the EB performed a flat-spin manoeuvre.

The EB consists of an experiment tank that contains approximately 2·7 kilograms of water, which is about 50% of the total volume of the tank. The experiment tank is an annular cylinder

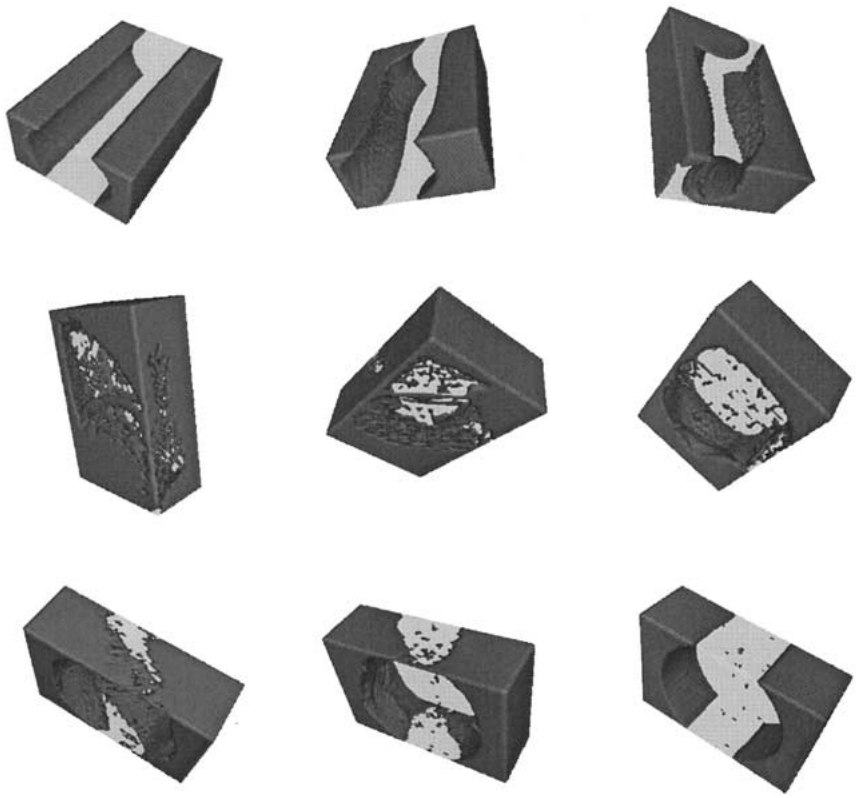

Figure 9. Three-dimensional snapshots (at unequal time intervals) of the flat-spin simulation with a filling ratio of 40%.

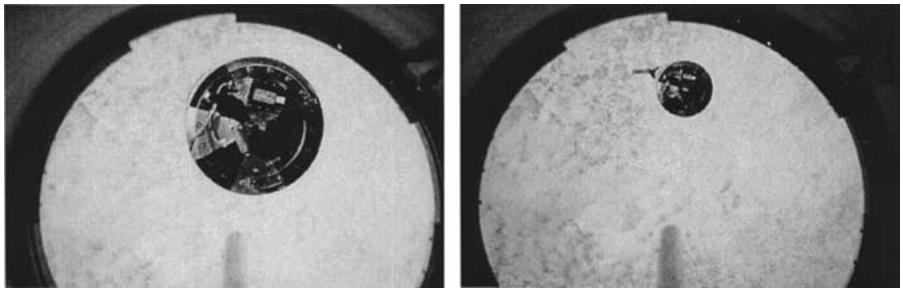

Figure 10. Photographs of the separation from MASER of the Ejectable Ballistometer taken during the Wet Satellite Model experiment (these photographs were taken from http://www.nlr.nl/public/hosted-sites/mgcd/EXPMNT/A-015.html).

of which the inner and outer radius are equal to 0·125 m and 0·145 m, respectively, and the height is equal to 0·323 m. The dry mass of the EB is 18·8 kg and its moment-of-inertia tensor equals diag (0·25, 0·38, 0·37) kg m^2. Since the annular width of the tank is much smaller than the axial and azimuthal dimensions of the tank, the radial velocity of the liquid can be neglected with respect to the axial and azimuthal velocities. Also, the radius of curvature in the radial direction is much smaller than the radius of curvature in the axial and azimuthal directions. Hence, the free surface will deform in the axial and/or azimuthal directions mainly and the flow can be assumed to be two-dimensional. This simplification to a two-dimensional

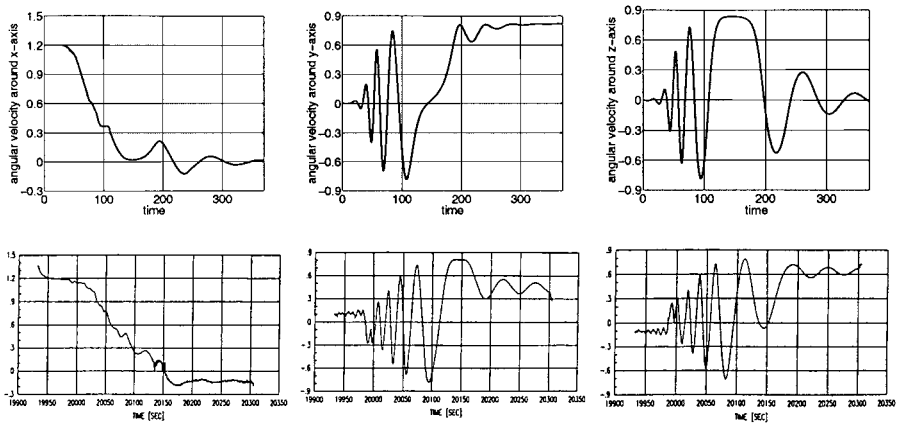

Figure 11. Angular velocities [s^{-1}] around x- (left), y- (middle) and z-axes (right) in the Wet Satellite Model experiment. Comparison of simulation (top) to experiment (bottom).

liquid dynamics problem was an important feature of the WSM experiment, since in 1992 no numerical models were available that could simulate a three-dimensional analogon of the WSM experiment.

When the EB was released from the MASER payload, its axis of symmetry was aligned with the direction of the separation push. Hence, all the liquid inside the experiment tank was initially located in the bottom side of the tank. The initial motion of the EB was induced by transferring angular momentum from a carried flywheel. The flywheel axis was aligned with the axis of symmetry, *i.e.*, the axis of minimum moment of inertia. Thus, the initial rotation of the EB was around this axis, whence a flat-spin transition could be expected. The amount of angular momentum transferred from the flywheel had been calibrated on the ground, such that the initial angular velocity around the axis of minimum moment of inertia was known accurately.

A simulation of the WSM experiment has been performed (actually the very first simulation of the WSM experiment). As in the experiment, the lower half of the annulus was filled with liquid and an initial angular velocity of 1·2 radians per second around the cylindrical axis was prescribed. For this simulation a grid consisting of $60 \times 60 \times 60$ cells was used and the time step, which was automatically adjusted based on the CFL number, varied from $\delta t = 2{\cdot}5 \times 10^{-4}$ s to $\delta t = 4 \times 10^{-3}$ s. The total simulation time was 370 seconds corresponding to the experiment time. Results from the simulation and the actual experiment are shown in Figure 11.

Although the geometry of the EB is not very suitable for a method based on Cartesian grids – a cylindrical grid would be more appropriate – the qualitative agreement between experiment and simulation is satisfactory. Indeed, the interval in which the angular velocity around the x-axis decreases from its initial value to zero is of the same order (approximately 200 seconds) in both the simulation and the experiment. Further, the frequencies of the oscillations in the angular velocities around the y- and z-axes in the simulations are comparable with those in the experiment. In particular the higher frequency oscillations in the first half and the lower frequency oscillations during the second half of the flat spin appear both in the experiment and the simulation. Also, the amplitude of the oscillations in the simulation is of the same magnitude as in the experiment. In the experiment, after about 200 seconds, the angular velocity around the y-axis is approximately constant for almost 40 seconds. This phenomenon

is also present in the simulation, however, not in the angular velocity around the y-axis but around the z-axis and somewhat earlier than in the experiment.

In the simulation, the angular velocity around the z-axis vanishes in the final stage of the flat spin. This behaviour is not visible in the experiment, where the EB seems to settle itself into a steady state where it is rotating both around the y- and z-axes. Since the rotation axis in the steady state depends on the moment-of-inertia tensor of the coupled system, and thus on the liquid distribution, apparently, the free-surface configuration that is predicted by the simulation does not agree with the experiment. Unfortunately, the free-surface configuration was not monitored during the WSM experiment. Hence, no further conclusions about this disagreement between simulation and experiment can be drawn.

5. Discussion

In this paper a method has been presented for the numerical simulation of coupled solid-liquid dynamics. The model consists of two parts. One part solves the liquid motion and another part takes care of the solid-body motion. Details of the numerical model for the solid-body dynamics have been presented in this paper.

The governing equations for the solid-body dynamics are naturally written in an inertial reference frame. Hence, the force and torque on the solid body due to the sloshing liquid also is written in this reference frame. However, discretisation of these equations results in a numerical method that is unstable if the liquid mass becomes too large with respect to the mass of the solid body. This has been demonstrated in a simulation of the free fall of a liquid-filled container. This stability problem was solved by decomposing the sloshing force and torque in two contributions.

The first contribution is the force and torque resulting from linear and angular accelerations of the fluid in the inertial reference frame, hereby neglecting the accelerations in the moving reference frame. The second contribution is the force and torque due to accelerations of the fluid in the moving reference frame only. The former contribution is then treated simultaneously with the motion of the solid body. Discretisation of this alternative mathematical model for the solid-body dynamics results in a numerical model that is stable for arbitrary liquid/solid mass ratios.

An important example of coupled solid-liquid dynamics is the flat-spin motion of a (partially) liquid-filled spacecraft. A flat-spin motion of a three-dimensional rectangular container partially filled with liquid has been simulated. This simulation showed that the numerical method can predict a flat spin correctly. A quantitative comparison of a flat spin was made by simulating the Wet Satellite Model (WSM) experiment. An adequate agreement between simulation and experiment was found.

Acknowledgements

J.G. wishes to acknowledge financial support from the Netherlands Organisation for Scientific Research (NWO-SRON). Also, the author wants to thank dr. Jan Vreeburg of the Nationals Aerospace Laboratory (NLR) in Amsterdam for providing the data of the WSM experiment.

References

1. W. Rumold, Modeling and simulation of vehicles carrying liquid cargo. *Multibody System Dynamics* 5 (2001) 351–374.
2. E.F.G. van Daalen, J. Gerrits, G.E. Loots, and A.E.P. Veldman, Free surface anti-roll tank simulations with a volume of fluid based Navier-Stokes solver. In: T. Miloh and G. Zilman (eds.), *Proceedings 15th International Workshop on Water Waves and Floating Bodies*, Caesarea, Israel, February 27 – March 1 (2000).
3. E.F.G. van Daalen, K.M.T. Kleefsman, J. Gerrits, H.R. Luth, and A.E.P. Veldman, Anti-roll tank simulations with a volume of fluid (VOF) based Navier-Stokes solver. In: *Twenty-Third Symposium on Naval Hydrodynamics*. Washington D.C.: National Academy Press (2001) pp. 457–473.
4. B. Iannotta, Slosh, rattle and roll. *New Scientist*, May 27 (2000) 32–35.
5. J. Gerrits, *Dynamics of Liquid-Filled Spacecraft*. Ph.D. thesis, University of Groningen, The Netherlands (2001) 112pp.
6. F.J. Kelecy and R.H. Pletcher, The development of a free surface capturing approach for multidimensional free surface flows in closed containers. *J. Comp. Phys.* 138 (1997) 939–980.
7. F.H. Harlow and J.E. Welch, Numerical calculation of time-dependent viscous incompressible flow of fluid with free surface. *Phys. Fluids* 8 (1965) 2182–2189.
8. D.K. Clarke, M.D. Salas, and H.A. Hassan, Euler calculations for multielement airfoils using Cartesian grids. *AIAA J.* 24 (1986) 353–358.
9. K. Morinishi, A finite difference solution of the Euler equations on non-body fitted Cartesian grids. *Comp. Fluids* 21 (1992) 331–344.
10. H.S. Udaykumar, H.-C. Kan, W. Shyy, and R. Tran-Son-Tay, Multiphase dynamics in arbitrary geometries on fixed Cartesian grids. *J. Comp. Phys.* 137 (1997) 366–405.
11. R.W.C.P. Verstappen and A.E.P. Veldman, Numerical computation of a viscous flow around a circular cylinder on a Cartesian grid. In: E. Oñate, G. Bugeda, and B. Suárez (eds.), *Proceedings ECCOMAS 2000*, Barcelona, Spain, September 11 – 14 (2000) paper 423.
12. C.R. Hirt and B.D. Nichols, Volume of fluid (VOF) method for the dynamics of free boundaries. *J. Comp. Phys.* 39 (1981) 201–225.
13. Z.A. Sabeur, J.E. Cohen, J.R. Stephens, and A.E.P. Veldman, Investigation on free-surface flow oscillatory impact pressures with the Volume-of-Fluid method. In: M.J. Baines (ed.), *Numerical Methods for Fluid Dynamics VI*. Oxford: Will Print (1998) pp.493–498.
14. J.P.B. Vreeburg, *The Wet Satellite Model Experiment*. Technical Report TP 94196 L, NLR, Amsterdam, The Netherlands (1994) 15pp.